Focused 70-cm Wavelength Radar Mapping of the Moon

Bruce A. Campbell, *Member, IEEE*, Donald B. Campbell, J. L. Margot, Rebecca R. Ghent,
Michael Nolan, John Chandler, Lynn M. Carter, and Nicholas J. S. Stacy

Abstract—We describe new 70-cm wavelength radar images of the lunar near-side and limb regions obtained via a synthetic-aperture-radar patch-focusing reduction technique. The data are obtained by transmitting a circularly polarized pulsed waveform from the Arecibo telescope in Puerto Rico and receiving the echo in both senses of circular polarization with the Robert C. Byrd Green Bank Telescope in West Virginia. The resultant images in both polarizations have a spatial resolution as fine as 320 m × 450 m near the lunar limb. The patch-focusing technique is a computationally efficient method for compensating for range migration and Doppler (azimuth) smearing over long coherence times, i.e., 983 s, which is needed to achieve the required Doppler resolution. Three to nine looks are averaged for speckle reduction and to improve the signal-to-noise ratio. At this long wavelength, the radar signal penetrates up to several tens of meters into the dry lunar surface materials, thus revealing details of the bulk loss properties and decimeter-scale rock abundance not evident in multispectral and other remote-sensing data. Application of the new radar images to the analysis of basalt flow complexes in Mare Serenitatis shows that the long-wavelength radar data are sensitive to differences in both flow age and composition, and may be particularly useful for studies of smaller deposits that do not have robust crater statistics. The new 70-cm lunar radar data are archived at the National Aeronautics and Space Administration Planetary Data System.

Index Terms—Moon, radar imaging.

I. INTRODUCTION

EARTH-BASED remote-sensing studies of the Moon include observations of ultraviolet, visible, and infrared (IR) reflectance; thermal IR properties during eclipse; and scattering or emission in the microwave region. Radar studies are of particular interest as the only method for probing to depths beyond a few centimeters (the range of thermal IR variations) and for their sensitivity to the bulk geochemical properties and rock abundance of the lunar regolith. Synoptic data sets for the Moon, which cover most of the visible near side, have been collected at wavelengths of 3.8 cm (2- to 4-km resolution) [1], 70 cm (4- to 8-km resolution) [2], and 7.5 m (10- to 30-km resolution) [3]. Selected areas have been mapped at spatial resolutions of 20–150 m using wavelengths of 3–4 cm [4]–[6] and 12.6 cm [7]–[9].

The 70-cm wavelength radar data have been proven to be particularly useful in probing the upper several meters of the regolith. Backscatter variations at this wavelength are correlated with the local and regional geologic properties, such as varying titanium content in mare basalts [10], [11], block-size distribution in ejecta from large craters and impact basins [12], [13], changes in bulk regolith loss tangent due to buried ancient mare basalt units [14], and rock-poor regional pyroclastic deposits formed by volcanic fire fountains [15]–[18]. There are strong reasons to conduct geologic studies at finer spatial resolution and to extend the 70-cm radar image coverage to areas near the poles and limbs that have previously not been investigated. To this end, we have collected data for a new 70-cm radar backscatter map of the Moon's near side with horizontal spatial resolution of 450–900 m.

Because of the large distances and relatively low resolution, the imaging of planetary bodies using Earth-based radars normally only requires unfocused processing of the data, which is usually referred to in the field of planetary radar astronomy as delay-Doppler mapping [19]. The 9-arcmin beamwidth of the Arecibo antenna is about 30% of the angular diameter of the Moon, so a single observation reveals a large field of view on the lunar surface. At the desired resolution of a few hundred meters, there is significant range migration and Doppler smearing at the edges of the field of view, which requires a focused reduction of the data. To minimize the computational effort, a simple focusing scheme [7] is implemented in which an unfocused delay-Doppler analysis followed by a coordinate transformation into selenographic coordinates is used to image a "patch" centered on a target location, i.e., the geographic point on the Moon for which the changing range and the range rate are compensated over the integration period (983 s). The patch size is dictated by the area over which the range and range–rate changes result in smearing of more than one-half of a resolution cell. A new target location is then chosen, and its computed range and phase history relative to the initial target location are used to focus the data at this point. Another delay-Doppler analysis is performed to obtain an image over the patch, and this process is repeated until the entire field of view is imaged. Sections II–V discuss the radar mapping and calibration methodology, while Section VI describes how

B. A. Campbell and L. M. Carter are with the Center for Earth and Planetary Studies, Smithsonian Institution, Washington, DC 20013-7012 USA (e-mail: campbellb@si.edu).

D. B. Campbell and J. L. Margot are with the Department of Astronomy, Cornell University, Ithaca, NY 14853 USA.

R. R. Ghent is with the Department of Geology, University of Toronto, Toronto, ON M5S 3B1, Canada.

M. Nolan is with the Arecibo Observatory, Arecibo, PR 00612, Puerto Rico.

J. Chandler is with the Smithsonian Astrophysical Observatory, Cambridge, MA 02138 USA.

N. J. S. Stacy is with the Defence Science and Technology Organization, Edinburgh, S.A. 5111, Australia.
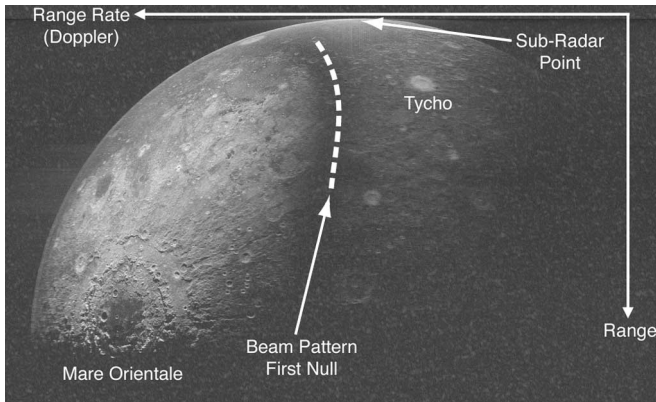
Fig. 1. Unfocused 70-cm wavelength delay-Doppler (range–rate) image of the Moon showing the radar illumination pattern on the surface. The dark curve marked in part by a white dashed curve is the first null of the Arecibo antenna beam pattern. The radar beam was centered on Mare Orientale (the dark region at the center of the Orientale basin).

radar echo information complements the estimation of mare basalt titanium content and age from multispectral and photographic data.

II. DATA COLLECTION

We transmit a left circularly polarized (LCP) radar signal at 430 MHz (radar wavelength λ of 0.7 m) from the 305-m National Science Foundation's (NSF's) Arecibo Telescope in Puerto Rico. The transmitted waveform is a 3-μs-long pulse at a pulse repetition period (PRP) of 15 ms, which yields a range resolution Δr of 450 m. The pulse repetition frequency (PRF) and its inverse (i.e., the PRP) must satisfy two conditions: 1) sample the frequency-broadened echo from the Moon at the relevant Nyquist frequency and 2) not exceed the delay depth of the Moon to avoid time ambiguity between successive pulses. The roundtrip time delay depth of the Moon (radius of 1738 km) is 11.59 ms, while the maximum apparent limb-to-limb bandwidth at 430 MHz is approximately 12 Hz. A PRF of 66.67 Hz (15-ms PRP) easily satisfies the ambiguity constraints and also provides data samples of a region "off the Moon" for system noise calibration measurements.

The reflected echoes in both circular polarizations are received at the 100-m NSF Robert C. Byrd Green Bank Telescope (GBT) in West Virginia and quadrature mixed to baseband (there are several mixing and filtering stages), and the resultant complex voltages are sampled at a 1-MHz rate [20] (Fig. 1). The GBT is used as the receiving station because the Arecibo 430-MHz monostatic radar system cannot receive the echo in both senses of circular polarization for nearby solar system targets such as the Moon, which has a roundtrip light time of about 2.5 s. Echoes polarized in the same circular sense as that transmitted (here LCP) are termed "SC" and often referred to as "depolarized" since they arise from effects such as multiple scattering or scattering from sharp edges. Echoes in the opposite circular sense (i.e., right circularly polarized) to that transmitted, i.e., the one expected for a mirror-like reflection, are termed "OC" or "polarized."

The GBT is not equipped to compensate in real time for changes in the range and range–rate (Doppler shift) to the target location (the beam center on the Moon), so these operations are performed at the transmitter in Arecibo. The echo from the target location thus arrives at the GBT at 430 MHz and with a PRP of 15 ms. The range and range–rate corrections are applied by simply Doppler shifting the transmitted signal and the 20-MHz clock that drives the timing generator. New values are applied at 1.0-ms intervals based on ephemerides, which are generated at the Smithsonian Astrophysical Observatory and predict the range and Doppler shift to the target location, plus the pointing information for the antennas, at 1-min intervals. A seventh-order polynomial is fitted to the Doppler shift values spanning the anticipated observation time and evaluated each time that the Doppler shifts are updated. A frequency offset of a few hertz (f_o) is added to the incoming signal at the GBT to move the center frequency of the lunar echoes away from 0 Hz to avoid problems related to DC level errors. During data acquisition, each quadrature channel is digitized using four-bit analog-to-digital conversion, and the resultant data stream is stored on a disk. The initial data analysis converts the four-bit samples to floating-point values and sums the 1-μs-spaced samples in pairs, which yields seven thousand five hundred 2-μs "range bins" per PRP. This retains a 50% oversampling of the 3-μs pulse. We further coherently sum groups of four individual PRPs, which yield an effective PRP of 60 ms (PRF of 16.67 Hz). Each radar coherence interval T_{coh} or "look" is 983 s long, which gives a frequency resolution of 1.017 mHz. Since the maximum limb-to-limb bandwidth of the Moon is approximately 12 Hz, there is a comfortable margin to avoid frequency aliasing. The presumming step introduces a $sinc^2$ variation in echo power with increasing frequency, which we correct in the subsequent mapping.

III. FOCUSED MAPPING

Each bistatic radar observation is made by tracking a particular target location on the Moon specified by a latitude θ_t and a longitude λ_t over a coherence interval sufficient to yield the required frequency resolution. As described in Section II, the time-varying range and range–rate for this point are corrected for in the transmitted signal so that the echo from the target arrives at the GBT at a fixed delay relative to the PRP and without a Doppler offset from 430 MHz. For all the other points on the Moon, however, the range and range–rate are changing with respect to the target point, with the rate of change increasing with distance from (θ_t, λ_t). A simple unfocused mapping of the radar echoes from the delay-Doppler coordinate system to a selenographic coordinate system will therefore lead to increased smearing in resolution with distance from the target point. We employ a "patch-focusing" algorithm to achieve the best possible spatial resolution across the region of the Moon illuminated by the 430-MHz Arecibo beam.

For almost all planetary radar observations, the beamwidths of the transmitting and receiving antennas (normally the same) are larger than the angular size of the solar system body being studied. This results in a north–south ambiguity; every location in one hemisphere of a rotating spherical body has a symmetric
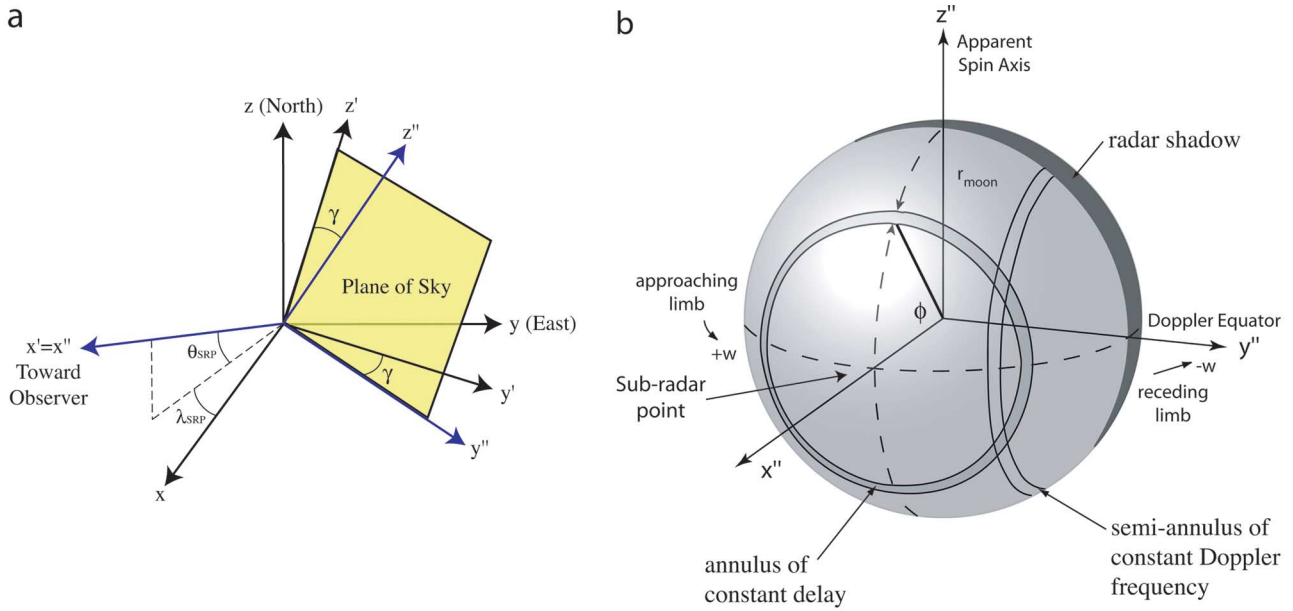
Fig. 2. Relationship between the lunar cartographic coordinate system (x, y, z) and the lunar range and range rate ("Doppler") coordinate system. (a) Diagram showing the two coordinate transformations discussed in the text. The first transformation places the x' axis along the line between the Moon's COM and the observer. After this rotation, the y' and z' axes define the "plane of the sky." A second rotation about the x' axis by the angle γ orients the z'' axis to match the direction of the Moon's apparent spin vector. (b) Diagram showing the projection of delay and Doppler shift variations onto the lunar surface. The line from the COM through the SRP defines the delay axis x''. The y'' axis corresponds to changes in the apparent range rate or Doppler shift. The Doppler "equator" lies in the $x''-y''$ plane; there is an ambiguity between delay and Doppler coordinates of points north and south of this plane. The radar incidence angle ϕ is defined with respect to the x'' axis.

location in the other hemisphere that has the same distance and velocity relative to the radar [19]. For a single observation, the echo powers from each pair of locations cannot be separated. For our lunar observations, the 9-arcmin beamwidth of the Arecibo antenna at 430 MHz is smaller than the 28-arcmin angular diameter of the Moon, thus allowing the ambiguity problem to be largely avoided by limiting the illuminated area to one lunar hemisphere.

The relative motion of an observer on the Earth and a point on the Moon has components due to the intrinsic rotations of the two bodies, the librations of the Moon, and the geometry of the observer–target line with respect to these components (Fig. 2). The subradar point (SRP), which is denoted by coordinates $(\theta_{\rm srp}, \lambda_{\rm srp})$, lies at the intersection of the lunar surface with a line between the observer and the Moon's center of mass (COM). The SRP moves on the surface of the Moon throughout an observation period, and a plane containing two successive SRP vectors and the COM defines the instantaneous "Doppler equator." The vector perpendicular to this plane at the COM represents the apparent instantaneous rotation axis or "Doppler axis" of the Moon.

Contours of equal radar time delay form concentric circles about the SRP, which are also contours of equal incidence angle for a spherical reference surface [Fig. 2(b)]. The Doppler shifts across the surface are well modeled by a spherical solid-body rotation for which the apparent rate and axial tilt vary with time. We may therefore express the Doppler shift for any given lunar surface point as a function of the instantaneous SRP, apparent plane-of-sky rotation angle for the Doppler axis γ [Fig. 2(a)], and apparent maximum Doppler shift at the limbs (in hertz) w.
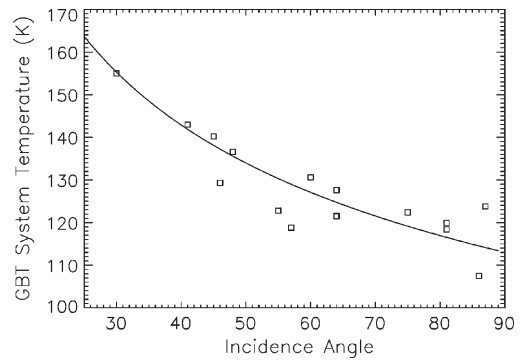

Fig. 3. Observed GBT 430-MHz system temperature (K), including lunar surface emission and background sky contributions, versus incidence angle for targets on the Moon. System temperature of about 166 K at the center of Moon and about 113 K at the limb. There is little dependence of lunar physical temperature on lunation at this wavelength. The solid line shows the best-fit power-law function of incidence angle for angles $> 25°$. The scatter in the data may be due to the radio-frequency interference at GBT, which varies in strength with time.

We can compute detailed range and frequency (phase) histories for any individual surface location relative to the target point, but carrying this out for thousands of surface locations to achieve focused mapping would be computationally intensive. One solution is to use range and range–rate information as a function of time for several points on the Moon. From these values, we determine a best-fit set of "spin" parameters at 1-min intervals ($\theta_{\rm srp}, \lambda_{\rm srp}, w$, and γ) and fit a second-order polynomial to their variation with time. The spin parameters are also used to set up the coordinate transformation between range and range–rate values, and the lunar latitude–longitude
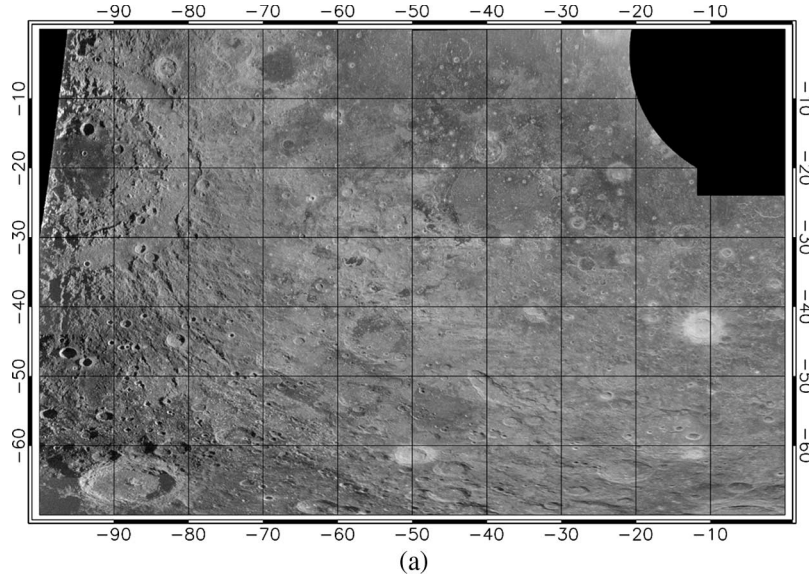
Fig. 4. Seventy-centimeter wavelength same-sense polarization radar image mosaics of the near-side and limb regions of the Moon. Radar echoes are normalized to a cosine variation of power with incidence angle. Logarithmic scaling with black–white dynamic range of 45 dB. Horizontal spatial resolution averaged to about 1.2 km per pixel. Simple cylindrical projection used for equatorial regions. (a) 70° S–0° N latitude; 100° W–0° W longitude.

grid. The interpolation errors introduced by using the spin parameters are below the values needed to create a one-pixel offset in the final selenographic maps.

The radar echoes are recorded as a time series of complex voltages denoted by $V(m, n)$, where m is the range bin, and n denotes the particular pulse record. The target point echo occurs at a fixed range bin m_t in all records and has zero frequency (or whatever arbitrary small offset value we introduce). To produce a delay-Doppler image about this point, we simply take the Fourier transform of the data along the columns (n) and resample to selenographic coordinates using the spin parameters (Section IV). No range compression is needed due to the use of a pulsed signal. As the distance from the target location increases, the range migration and Doppler offset over the 983-s coherence interval also increase. The distance over which this offset becomes comparable to the range and/or frequency resolution defines a "patch size" [7].

We build up the output map of a particular illuminated region by carrying out the frequency-transform operation and selenographic resampling for constituent patches after applying a time-varying correction to the raw data array for delay and frequency variations between the original target point (θ_t, λ_t) and the center of the patch (a method suggested in [7]). The focusing operation is applied in four steps. 1) An interpolation of each range record (along the m time samples) is used to correct the time-varying delay offset. These delay errors vary slowly with time, so we can apply a single correction to each pulse record. 2) The cumulative phase difference between the pointing target and the patch center, i.e., the primary source of image smearing, is compensated at each pulse record of the complex voltage array based on the spin state of the Moon at the start of the pulse. 3) The array is Fourier transformed along the frequency lines to yield a delay-Doppler array. 4) The relative backscatter intensity is mapped to selenographic coordinates across the patch, as detailed in the next section.

IV. RELATIONSHIP OF DELAY-DOPPLER AND SELENOGRAPHIC COORDINATES

The mapping between delay-Doppler and selenographic coordinates requires a transform between the Cartesian (x, y, z) location of a point on the lunar reference grid with latitude θ and longitude λ

$$\begin{bmatrix} x \\ y \\ z \end{bmatrix} = r_{\text{moon}} \begin{bmatrix} \cos\theta \cos\lambda \\ \cos\theta \sin\lambda \\ \sin\theta \end{bmatrix} \tag{1}$$

and the (x'', y'', z'') coordinates along the axes that define the apparent (plane of sky) orientation and spin state of the Moon (Fig. 2). The radius of the Moon at this location is given by r_{moon}. For most mapping, we assume a single mean radius for the Moon, but a more detailed topography (if available) could be used to orthorectify the final image. The transformation is represented by

$$[D][S] \begin{bmatrix} x \\ y \\ z \end{bmatrix} = \begin{bmatrix} x'' \\ y'' \\ z'' \end{bmatrix} \tag{2}$$

where $[S]$ rotates the coordinate system to place the SRP along the $x' = x''$ axis as

$$[S] = \begin{bmatrix} \cos\lambda_{\text{srp}} \cos\theta_{\text{srp}} & \sin\lambda_{\text{srp}} \cos\theta_{\text{srp}} & \sin\theta_{\text{srp}} \\ -\sin\lambda_{\text{srp}} & \cos\lambda_{\text{srp}} & 0 \\ -\cos\lambda_{\text{srp}} \sin\theta_{\text{srp}} & -\sin\lambda_{\text{srp}} \sin\theta_{\text{srp}} & \cos\theta_{\text{srp}} \end{bmatrix}. \tag{3}$$

The $[D]$ matrix rotates the coordinates about the $x' = x''$ axis by the Doppler angle (defined as positive clockwise) γ as

$$[D] = \begin{bmatrix} 1 & 0 & 0 \\ 0 & \cos\gamma & -\sin\gamma \\ 0 & \sin\gamma & \cos\gamma \end{bmatrix}. \tag{4}$$
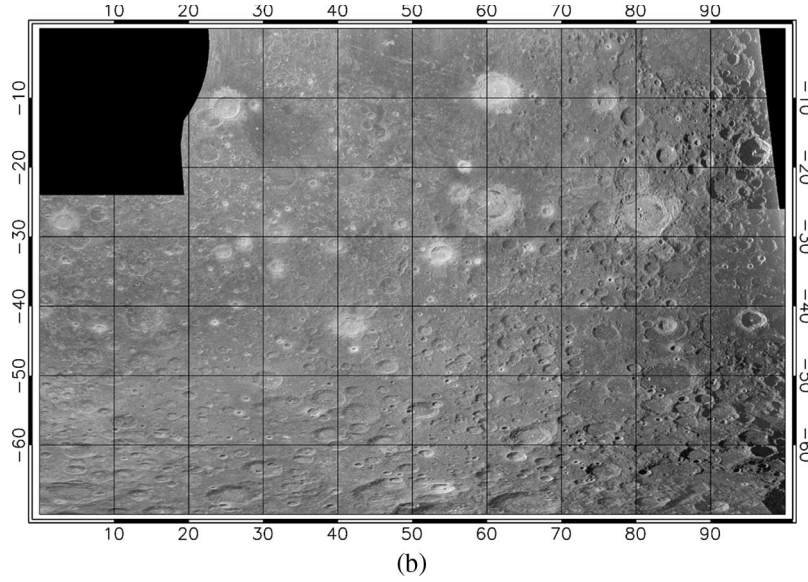
(b)

Fig. 4. (*Continued.*) Seventy-centimeter wavelength same-sense polarization radar image mosaics of the near-side and limb regions of the Moon. Radar echoes are normalized to a cosine variation of power with incidence angle. Logarithmic scaling with black–white dynamic range of 45 dB. Horizontal spatial resolution averaged to about 1.2 km per pixel. Simple cylindrical projection used for equatorial regions. (b) 70° S–0° N latitude, 0° E–100° E longitude.

Delay variations arise due to differences in the range of a surface point R_T at (x'', y'', z'') with respect to the SRP range R_{srp}. This difference in range is given by

$$
\begin{aligned}
\Delta r &= R_T - R_{\mathrm{srp}} \\
&= \left[R_{\mathrm{srp}}^2 + 2r_{\mathrm{moon}}^2 + 2R_{\mathrm{srp}}r_{\mathrm{moon}} \right. \\
&\quad \left. - 2x''(R_{\mathrm{srp}} + r_{\mathrm{moon}}) \right]^{1/2} - R_{\mathrm{srp}}
\end{aligned}
\tag{5}
$$

and the appropriate delay bin is

$$
n\_delay = m_o - \frac{2\Delta r}{\Delta t c}
\tag{6}
$$

where c is the speed of light, and Δt is the delay resolution. The value of x'' must be > 0 in order for the desired point to be on the radar-visible hemisphere of the Moon. The radar incidence angle ϕ is [Fig. 2(b)]

$$
\phi = \cos^{-1}(x''/r_{\mathrm{moon}}).
\tag{7}
$$

The frequency bin in the transformed data array for a surface point at (x'', y'', z'') is

$$
n\_freq = T_{\mathrm{coh}}(f_o + y''^*w/r_{\mathrm{moon}})\frac{(R_{\mathrm{srp}} + r_{\mathrm{moon}})}{R_T}.
\tag{8}
$$

We reproject the radar data by solving for the appropriate delay and frequency bin in the Fourier-transformed array for each (latitude, longitude) cell in the output map. These output values may be complex valued, if we wish to later form a Stokes' vector representation of the echo, or converted to relative power by taking the squared magnitude of the complex values.

The surface horizontal resolution along the range axis is a function of the incidence angle

$$
\Delta s_{\mathrm{range}} = \Delta r / \sin \phi = \frac{c\Delta t}{2\sqrt{1 - \left(\frac{x''}{r_{\mathrm{moon}}}\right)^2}}
\tag{9}
$$

and for our 3-μs observations, it varies from 450 m at the limbs to 900 m at 30° incidence. The horizontal resolution along the axis perpendicular to the range direction ("azimuth") $\Delta s_{\mathrm{azimuth}}$ is best when the image area is close to the Doppler axis $(y'' = 0)$

$$
s_{\mathrm{azimuth}} = \frac{r_{\mathrm{moon}}}{wT_{\mathrm{coh}}\sqrt{1 - \left(\frac{y''}{r_{\mathrm{moon}}}\right)^2}}.
\tag{10}
$$

The surface area A contributing to the echo in a given delay-Doppler cell is thus

$$
A = \frac{r_{\mathrm{moon}}c\Delta t}{2wT_{\mathrm{coh}}\sqrt{1 - \left(\frac{x''}{r_{\mathrm{moon}}}\right)^2}\sqrt{1 - \left(\frac{y''}{r_{\mathrm{moon}}}\right)^2}}.
\tag{11}
$$

For the 983-s looks, the finest possible azimuth horizontal resolution is about 320 m. Farther from the axis, the azimuth resolution cells increase in size, and at the Doppler equator (where the azimuth and range axes are parallel), there is no useful frequency mapping capability. The final maps are produced at 400-m resolution to limit undersampling of the frequency-resolved cells.

V. CALIBRATION AND MULTILOOK AVERAGING

One advantage of our 70-cm radar mapping relative to shorter-wavelength observations using the same antennas is the large illuminated region on the Moon. This permits the
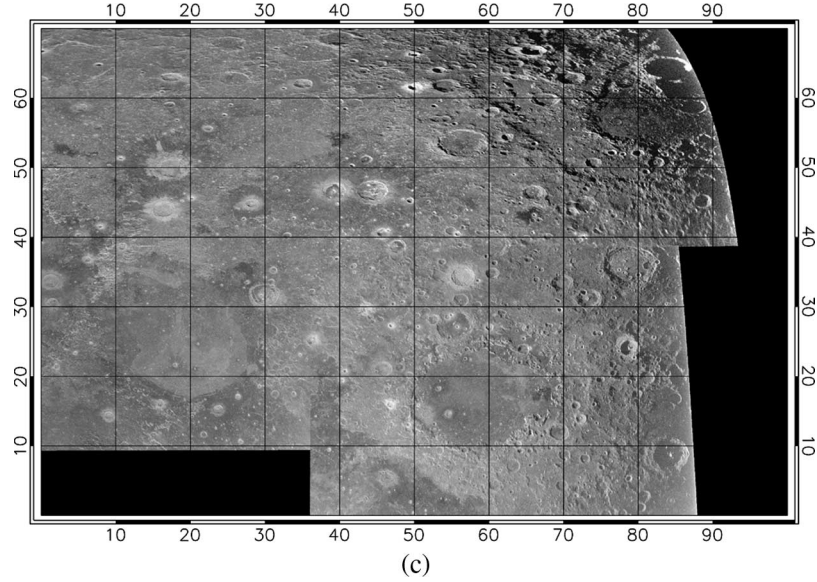
Fig. 4. (*Continued.*) Seventy-centimeter wavelength same-sense polarization radar image mosaics of the near-side and limb regions of the Moon. Radar echoes are normalized to a cosine variation of power with incidence angle. Logarithmic scaling with black–white dynamic range of 45 dB. Horizontal spatial resolution averaged to about 1.2 km per pixel. Simple cylindrical projection used for equatorial regions. (c) 0° N–70° N latitude, 0° E–100° E longitude.

acquisition of full near-side coverage (with three or more looks) in about 20 runs (one run is a 2- to 2.5-h passage of the Moon above Arecibo) with different target locations. There is however a variation in effective gain across the illuminated region (Fig. 1), which must be removed to mosaic data for adjacent target areas. The true beam pattern varies with time during a run because the Arecibo 430-MHz line feed illuminates a toroidal region of the dish and progressively spills off the edge of the fixed reflector as the elevation angle decreases. The GBT antenna has a fixed sensitivity pattern as it tracks the target point. The net roundtrip power beam pattern $P(\kappa)$, which represents the product of the individual Arecibo and GBT patterns for a summed set of looks, can be represented by a Bessel function with an "effective width" parameter W as

$$P(\kappa) = [J_1(2W\pi \sin \kappa)/(W\pi \sin \kappa)]^4 \qquad (12)$$

where κ is the angle between the pointing target and a chosen surface point [21]. In the case of a fully illuminated aperture at Arecibo (i.e., when pointing at the zenith), the net beam pattern is well represented by $W = 170$. Lower values correspond to wider beams as the illuminated area of the Arecibo antenna decreases with decreasing elevation angle. The beam angle may be defined from the plane-of-sky offsets in the rotated coordinate system and the observer–target distance R_T as

$$\kappa = \tan^{-1}\left(\frac{\sqrt{\left(y'' - y''_{\text{target}}\right)^2 + \left(z'' - z''_{\text{target}}\right)^2}}{R_T}\right). \qquad (13)$$

The average beam pattern for the Arecibo–GBT 70-cm data is given by $W = 155$ based on the analysis of overlap regions between images collected for different pointing centers. The resulting correction factor (12) is used to normalize the σ° values for their distance from the beam center.

Every 15-ms data record includes a 3.41-ms interval that contains no reflections from the Moon. For this interval, the measured power equals the product of the net system gain in each channel (G_1 and G_2) and the net thermal noise from the receiver system, Moon, and background sky. The degree to which the Moon fills the GBT beam varies with the target location on the lunar surface. The lunar and sky emissions are assumed to be the same in the two circular polarizations. Where lunar echoes are present, the measured power contains both the noise and the lunar echo power. The dimensionless backscatter coefficient σ° may be expressed in terms of the average transmitted power P_T, thermal noise power P_N, scattering area A, gain of the transmitting and receiving antennas G_{AO} and G_{GBT}, range between the target and the observer R_T, and ratio of the observed echo power (i.e., after the off-Moon noise power has been subtracted) at some location in the radar image S_{image} to that in the off-Moon region $S_{\text{off-Moon}}$

$$\sigma^o = \frac{S_{\text{image}}}{S_{\text{off-Moon}}} \left(\frac{P_N}{P_T}\right) \left(\frac{1}{A}\right) \left[\frac{64\pi^3 R_T^4}{\lambda^2 G_{\text{AO}} G_{\text{GBT}}}\right]. \qquad (14)$$

The noise power is given by $kT_B B_N$, where k is Boltzmann's constant, T_B is the system temperature of the GBT at 430 MHz, and B_N is the noise bandwidth.

The system temperature varies with the degree to which the Moon fills the GBT beam, so we measured this parameter as a function of incidence angle for the center of the pointing region (i.e., from the center of the Moon to the limbs). We also observed a sky source of known flux at 430 MHz to calibrate the GBT system temperature. As expected, the system temperatures were very similar between the left and right circular polarization receivers, and the average value is 166 K when the GBT is pointed at the center of the Moon. Since none of our mapping observations have a target incidence angle less than about 30°, we did not fully characterize the slow change in system temperature between $\phi = 0°$ and $\phi = 25°$. At
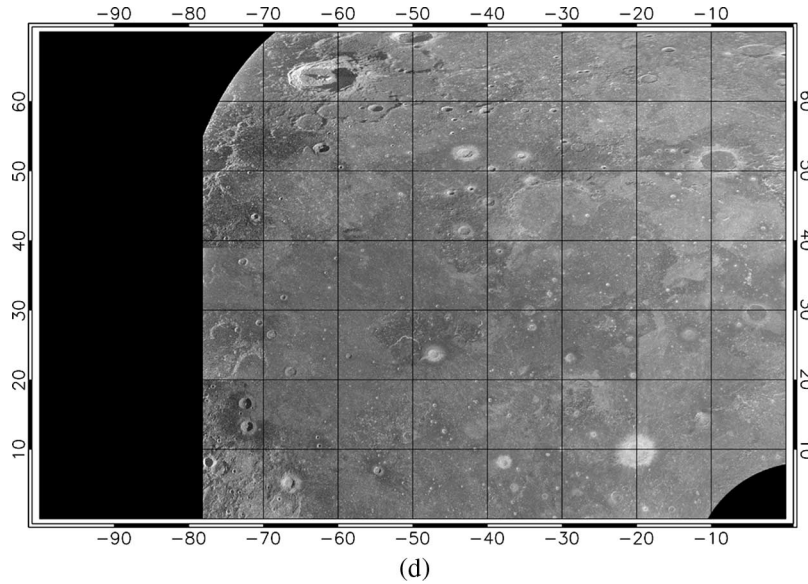
Fig. 4.   (*Continued.*) Seventy-centimeter wavelength same-sense polarization radar image mosaics of the near-side and limb regions of the Moon. Radar echoes are normalized to a cosine variation of power with incidence angle. Logarithmic scaling with black–white dynamic range of 45 dB. Horizontal spatial resolution averaged to about 1.2 km per pixel. Simple cylindrical projection used for equatorial regions. (d) 0° N–70° N latitude, 0° W–100° W longitude.

higher angles, the beam is partially off the Moon, and a good approximation to the GBT system temperature is

$$T_{\text{system}}^{\text{GBT}} = 415\phi^{-0.289}(\phi > 25^0). \qquad (15)$$

Targets very close to the limb thus have a noise temperature of about 113 K (Fig. 3).

The noise bandwidth is very close to the frequency resolution of 1.017 MHz. The gain of the GBT at 430 MHz is a fixed value (51.5 dB), but the dependence of the illuminated area on the Arecibo primary reflector on zenith angle leads to a reduction in gain with zenith angle α in degrees (P. Perillat, personal communication), i.e.,

$$G_{\text{AO}} = \left(\frac{11044\pi}{\lambda^2}\right)[18.67 - 0.5414\alpha]. \qquad (16)$$

Using these corrections, the derived σ° values in spatially overlapping regions of observations with different target locations differ by ± 3 dB. Our greatest uncertainty in calibrating the backscatter coefficient is the transmitted power, which is not well measured at Arecibo. These differences between different observation runs can be compensated to produce mosaics of large areas (Fig. 4), but the absolute backscatter coefficient remains uncertain by about 50%. The relative cross sections between the two circular polarizations are known with much higher accuracy.

To decrease speckle noise in the final radar maps, we collect three or more independent looks at each target area. Each look is mapped using the patch-focusing method. Slight image distortions between looks are corrected by selecting a single look as a reference image and choosing widely spaced tie points within this image. For each succeeding look, we determine through cross correlation the best offset $(\Delta x, \Delta y)$ for each tie point, apply a rubbersheet transformation, and sum the data. The standard deviation of the relative power values due to speckle is reduced by incoherent summation as $1/\sqrt{N}$,

where N is the number of averaged looks. While three or more summed looks yield a geologically useful radar map, we typically require a higher degree of local averaging (100 looks or more) to reduce the uncertainties in the circular polarization ratio (CPR) (SC/OC power).

The 70-cm radar maps are archived at the National Aeronautics and Space Administration (NASA) Planetary Data System (PDS) in two formats. The "NASA Level 1" data (PDS Level 4) are in the form of backscattered power (in each of the two received senses of circular polarization) normalized to the thermal noise in each look and the scattering area of every resolution cell on the surface, projected to a latitude–longitude grid, and averaged over three to nine looks. Maps of the equatorial and midlatitudes are presented in a sinusoidal equal-area projection. Areas at higher latitude are shown in polar stereographic projection. The "NASA Level 2" data (PDS Level 5) are calibrated to our best estimate of the absolute backscatter coefficient, normalized to the measured 68-cm scattering functions in [22] to reduce the strong dependence of echo brightness on incidence angle, and geometrically warped to match the Clementine 750-nm lunar image base produced by the U.S. Geological Survey. Level 2 products also include a CPR data set formed after averaging the echo data for the two circular polarization channels to 2-km resolution (at least 75 total averaged looks per pixel).

VI. RELATIONSHIP OF RADAR ECHOES TO MARE BASALT AGE AND ILMENITE CONTENT

Basins on the lunar near side, which are formed by giant impacts more than 2.8 billion years (b.y.) ago, are largely filled by basaltic lava flows called maria. These flow complexes formed as low relief plains and have been subsequently covered by an impact-produced mixture of rocky debris and dust called the regolith. Considerable work has been done to understand mare composition and age, since these reveal the thermal and
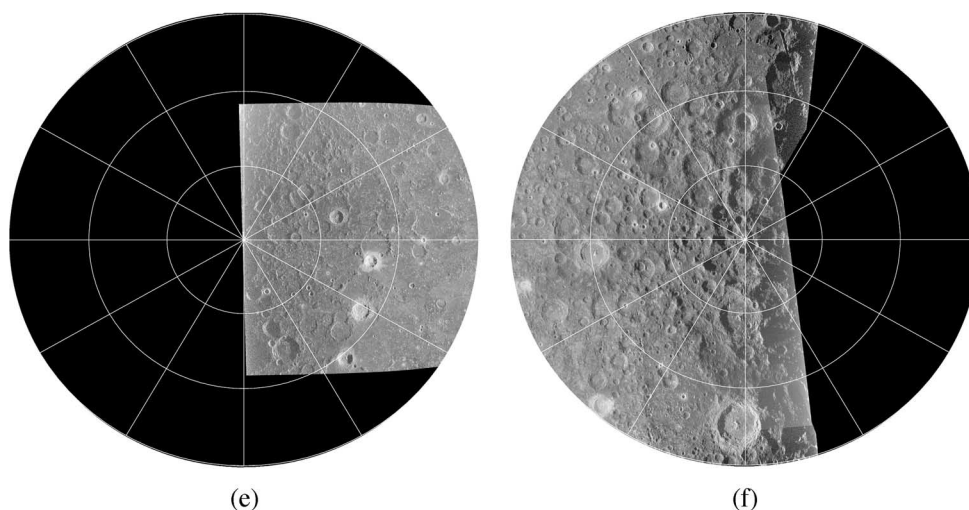
(e) (f)

Fig. 4. (*Continued.*) Seventy-centimeter wavelength same-sense polarization radar image mosaics of the near-side and limb regions of the Moon. Radar echoes are normalized to a cosine variation of power with incidence angle. Logarithmic scaling with black–white dynamic range of 45 dB. Horizontal spatial resolution averaged to about 1.2 km per pixel. Simple cylindrical projection used for equatorial regions. (e) Polar stereographic projection of the north polar region ($60°$–$90°$ N latitude). Zero longitude is toward the right. (f) Polar stereographic projection of the south polar region ($60°$–$90°$ S latitude). Zero longitude is toward the left. Note that the Moon's libration during the period 2002–2006 predominantly favored viewing of the southern hemisphere from Arecibo. As a result, the spatial coverage of the northern hemisphere is more limited in longitude.

chemical history of the magma reservoirs that supplied the eruptions. There are two principal sources of remote-sensing information on mare flow composition: near-IR multispectral properties and orbital gamma-ray/neutron spectroscopy. Relative dating is accomplished by studying the abundance and degradation state of impact craters, with absolute dating by reference to population curves for areas surrounding samples of known age. As a general rule, crater–population age estimates are most robust where large regions are studied, and have greater possible errors for smaller areas. Two recent studies [23], [24] applied these techniques to spectroscopically defined units across most near-side maria.

Long-wavelength radar data can play a complementary role in these investigations. Schaber *et al.* [10] noted that the 70-cm radar echoes for lava flows in Mare Imbrium were typically lower for flows that are "blue," or higher in their abundance of the mineral ilmenite ($FeTiO_3$). This mineral has a higher microwave loss tangent than other species in mare basalts and much higher loss than the generally feldspar-rich rocks that form the lunar highlands; work on returned lunar samples confirmed that the loss properties of basalts are correlated with the total iron and titanium content [25]. Since much of the 70-cm radar return comes from scattering within the regolith, an increased loss tangent leads to lower echoes by attenuating the incident signal [26].

Comparison of the 4- to 8-km-resolution 70-cm radar images with FeO and TiO_2 abundance estimated from multispectral data showed that the TiO_2 (i.e., ilmenite) content appears to be the principal driver of basalt loss tangents, with the other iron-bearing minerals playing a much less significant role [11]. This same study identified differences in overall radar brightness between the maria in major basins for any given TiO_2 abundance and suggested that such variations might be linked to relative age. In this model, supported by measurements of the thermal properties of the maria during eclipse, younger mare units have a thin (2–3 m) regolith cover, which permits relatively small
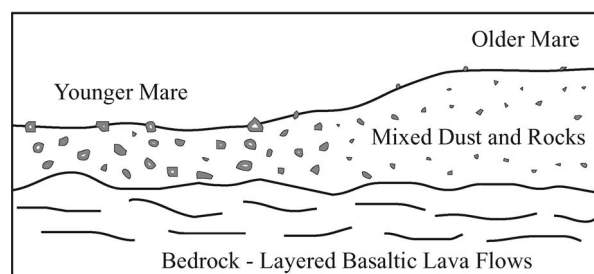

Fig. 5. Cartoon representation of the mare regolith thickness and rock abundance variations with age. The younger mare regolith is thinner (2–3 m) and has a larger population of suspended and surface decimeter-scale rocks. The older mare regolith is thicker (5–8 m) and has fewer 10-cm and larger-diameter rocks capable of supporting 70-cm radar scattering.

impacts to excavate fresh blocky debris from the underlying bedrock. With greater age, the regolith thickens to 5–8 m, and small impacts simply break down the existing suspended boulders. As a result, a younger mare unit will have a higher radar brightness (more surface and suspended rocks to permit volume scattering) than an older unit of the same TiO_2 content (Fig. 5). Our new 70-cm radar maps permit a more detailed comparison between echo properties, inferred composition, and crater–statistic age estimates.

We selected Mare Serenitatis [Fig. 6(a)] for a preliminary study as the entire basin is contained within a single beam pattern of the 70-cm system [Fig. 6(b)]. This avoids any issues of relative calibration between images collected with different target centers. Serenitatis basalts were mapped based on differences in IR reflectance by Pieters [27] and in an early form by Thompson *et al.* [28]. We mapped the FeO [Fig. 6(c)] and TiO_2 [Fig. 6(d)] abundance using Clementine data (available from the PDS) and the techniques of Lucey *et al.* [29] and Gillis *et al.* [30]. The ages of mare units within Serenitatis (based on crater statistics) range from 2.44 to 3.81 b.y. For comparison, the basalts across the near side of the Moon range from
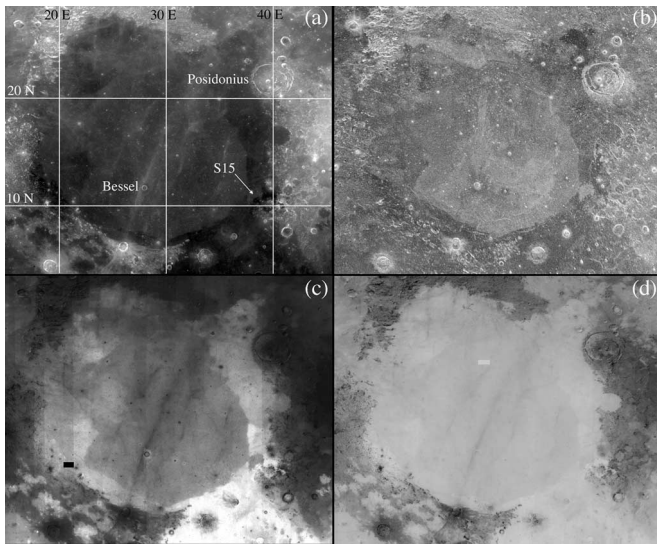
Fig. 6. (a) Clementine 750-nm mosaic of Mare Serenitatis. The region covered is $12.8° - 39.8°$ N, $3.1° - 35.3°$ E. (b) Seventy-centimeter SC-polarized radar image of Mare Serenitatis. (c) Map of TiO_2 content across Serenitatis using Clementine multispectral data and the technique of Gillis *et al.* [2003]. The black–white stretch corresponds to values of 0%–15%. (d) Map of FeO content across Serenitatis using Clementine multispectral data and the technique of Lucey *et al.* [2000]. The black–white stretch corresponds to values of 0%–25%.
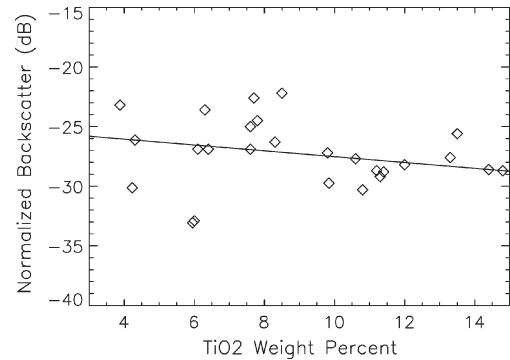

Fig. 7. Plot of radar backscatter versus TiO_2 content for basalts in Mare Serenitatis. The solid line shows the best-fit trend for all sites. The slope of the trend line is -0.24 dB per weight percent TiO_2.
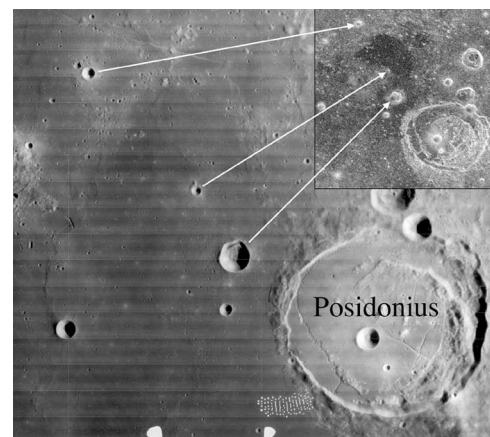

Fig. 8. Lunar Orbiter IV view of the area that is north of Posidonius crater (95-km diameter), and (inset) 70-cm same-sense radar image of similar area, which shows a very low backscatter from an apparently older mare flow unit. White arrows connect crater locations in both images for reference.

a minimum age of about 1.2 b.y. to a maximum age of just over 3.9 b.y. [24].

Mare Serenitatis is characterized by an inner area of lower titanium and iron basalts, and surrounded by a concentric ring of moderate to high titanium flows. Many of the abrupt changes in TiO_2 between flow complexes are accompanied by changes in the same sense radar echo, which is consistent with our expectation that ilmenite modulates the regolith loss tangent. However, a comparison of the radar image and TiO_2 map also shows some dramatic differences. Most striking is a "finger" of radar-bright material extending northward from the area of Bessel crater. This higher radar return is not accompanied by a change in the iron or titanium maps. In the area northwest of Posidonius crater, a relatively homogenous region of moderate TiO_2 flows comprises distinct areas of moderate and very low radar return. Across the entire Serenitatis basin, the radar echoes appear to trace "unit" boundaries that are often somewhat different from those that are readily noted in the TiO_2 map or in earlier multispectral characterizations [27].

To illustrate these differences, we compared the average same-sense radar brightness to the average TiO_2 abundance for 25 sample areas with relatively uniform properties (Fig. 7). Based on earlier studies and a model for the dependence of 70-cm echoes on the ilmenite content of the regolith, we expect about a 0.3-dB decline in echo power for each 1% rise in TiO_2 content. This corresponds to about one-half of the echo power arising from within the regolith—if all of the echoes come from the subsurface, we expect about 0.6 dB of change per weight percent TiO_2 [14]. The data shown in Fig. 7 are best fit by a linear function with slope of -0.24 dB per 1% TiO_2, but there is a range in backscatter of about ± 5 dB about this line for any given titanium content.

Some of the spread in echo power with respect to the best-fit line is likely related to the differences in age and the associated variation in regolith thickness and rock abundance (Fig. 5) relative to the average age across all of the sampled areas (about 3.4 b.y.). A feature that may be older than the average is north of Posidonius (Fig. 8). This radar-dark area has an echo strength that is 5 dB lower than the neighboring deposit (termed as S8 by Hiesinger *et al.* [23] and dated to 3.63 b.y.) of similar TiO_2 content. A possible area with younger age than expected is part of unit S15, which was estimated at 3.44 b.y. [23] [labeled in Fig. 6(a)]. In the southeastern portion of this unit, the radar echo is 5 dB higher than predicted from the TiO_2 content, which suggest that materials near the basin rim are younger than the more interior deposits of similar spectral properties.

Our preliminary analysis of the differences in radar backscatter between units of similar TiO_2 content with ages based on crater statistics [23] did not show a strong correlation of greater age with lower backscatter. However, such a test is not robust for two reasons. First, the 25 sites chosen for the radar versus TiO_2 study (Fig. 7) often do not overlap the limited areas chosen for crater counting in [23], so there could be differences in age between our sites not resolved by that study. For example, the two extreme cases noted above were not sampled for statistical analysis in [23]. Second, some radar-identified units within

Mare Serenitatis are not matched by changes in spectroscopic properties (Fig. 6), which suggests that larger crater-count sample boxes could mix terrains of different age. It is also possible that discrepancies in radar return from a simple trend with TiO_2 may arise from mineralogic differences that cause significant variations in the microwave loss tangent among rocks with similar FeO and TiO_2 abundance. At present, we have no strong evidence for such a mineralogical mechanism based on lab studies of lunar rocks [25], but the sample collection is not necessarily complete with regard to possible basalt compositions.

Further work is needed to examine crater counts in relatively large areas of uniform TiO_2 content and to compare these with the average radar echo behavior to 1) define a relationship between σ°, TiO_2, and age, and 2) identify basalt deposits that appear to have anomalous mineralogy. If this technique proves valid, then the radar data and inferred composition could be used to define relative ages for mare outcrops too small for robust crater statistics.

VII. CONCLUSION

The new 70-cm wavelength radar maps have application to studies of lunar geologic history; the resource potential of mare basalts, pyroclastic deposits, and polar cold traps [31]; and the search for safe landing areas. These data are archived at the NASA PDS to make them available to the lunar science community [32].

ACKNOWLEDGMENT

REFERENCES

[1] S. H. Zisk, G. H. Pettengill, and G. W. Catuna, "High-resolution radar maps of the lunar surface at 3.8-cm wavelength," *Earth Moon, Planets*, vol. 10, no. 1, pp. 17–50, May 1974.

[2] T. W. Thompson, "High-resolution lunar radar map at 70-cm wavelength," *Earth Moon, Planets*, vol. 37, no. 1, pp. 59–70, Jan. 1987.

[3] T. W. Thompson, "High resolution lunar radar map at 7.5 m wavelength," *Icarus*, vol. 36, pp. 174–188, Nov. 1978.

[4] S. H. Zisk, B. A. Campbell, G. H. Pettengill, and R. Brockelman, "Alphonsus crater: Floor fracture and dark-mantle deposit distribution from new 3.0-cm radar images," *Geophys. Res. Lett.*, vol. 18, pp. 2137–2140, Nov. 1991.

[5] J. L. Margot, D. B. Campbell, R. F. Jurgens, and M. A. Slade, "Topography of the lunar poles from radar interferometry: A survey of cold trap locations," *Science*, vol. 284, no. 5420, pp. 1658–1660, Jun. 1999.

[6] J. L. Margot, D. B. Campbell, R. F. Jurgens, and M. A. Slade, "Digital elevation models of the Moon from Earth-based radar interferometry," *IEEE Trans. Geosci. Remote Sens.*, vol. 38, no. 2, pp. 1122–1133, Mar. 2000.

[7] N. J. S. Stacy, "High-resolution synthetic aperture radar observations of the moon," Ph.D. dissertation, Cornell Univ., Ithaca, NY, 1993.

[8] N. J. S. Stacy, D. B. Campbell, and P. G. Ford, "Arecibo radar mapping of the lunar poles: A search for ice deposits," *Science*, vol. 276, no. 5318, pp. 1527–1530, Jun. 1997.

[9] D. B. Campbell, B. A. Campbell, L. M. Carter, J. L. Margot, and N. J. S. Stacy, "Lunar polar ice: No evidence for thick deposits at the South Pole," *Nature*, vol. 443, pp. 835–837, 2006.

[10] G. G. Schaber, T. W. Thompson, and S. H. Zisk, "Lava flows in Mare Imbrium: An evaluation of anomalously low Earth-based radar reflectivity," *Moon*, vol. 13, pp. 395–423, 1975.

[11] B. A. Campbell, B. R. Hawke, and T. W. Thompson, "Long-wavelength radar studies of the lunar maria," *J. Geophys. Res.*, vol. 102, pp. 19 307–19 320, 1997.

[12] T. W. Thompson, W. J. Roberts, W. K. Hartmann, R. W. Shorthill, and S. H. Zisk, "Blocky craters: Implications about the lunar megaregolith," *Earth Moon, Planets*, vol. 21, no. 3, pp. 319–342, Nov. 1979.

[13] R. R. Ghent, D. W. Leverington, B. A. Campbell, B. R. Hawke, and D. B. Campbell, "Earth-based observations of radar-dark crater haloes on the Moon: Implications for regolith properties," *J. Geophys. Res.*, vol. 110, no. E2, E02005, 2005. DOI:10.1029/2004JE002366.

[14] B. A. Campbell and B. R. Hawke, "Radar mapping of lunar cryptomaria east of Orientale basin," *J. Geophys. Res.*, vol. 110, no. E9, E09002, 2005. DOI:10.1029/2005JE002425.

[15] S. H. Zisk, C. A. Hodges, H. J. Moore, R. W. Shorthill, T. W. Thompson, E. A. Whitaker, and D. E. Wilhelms, "The Aristarchus–Harbinger region of the moon: Surface geology and history from recent remote sensing observations," *Earth Moon, Planets*, vol. 17, no. 1, pp. 59–99, Sep. 1977.

[16] L. R. Gaddis, C. M. Pieters, and B. R. Hawke, "Remote sensing of lunar pyroclastic mantling deposits," *Icarus*, vol. 61, no. 3, pp. 461–489, Mar. 1985.

[17] B. A. Campbell, N. J. S. Stacy, D. B. Campbell, S. H. Zisk, and T. W. Thompson, "Estimating lunar pyroclastic deposit depths from imaging radar data: Applications to lunar resource assessment," in "*Proc. Workshop New Technol. Lunar Resource Assessment*," pp. 16–17, 1992. LPI Tech. Rep. 92-06.

[18] B. A. Campbell, D. B. Campbell, J. L. Margot, R. R. Ghent, M. Nolan, L. M. Carter, and N. J. S. Stacy, "Looking below the Moon's surface with radar," *EOS Trans. AGU*, vol. 88, no. 2, pp. 13–18, 2007.

[19] G. H. Pettengill, S. H. Zisk, and T. W. Thompson, "The mapping of lunar radar scattering characteristics," *Earth Moon, Planets*, vol. 10, no. 1, pp. 3–16, May 1974.

[20] J. L. Margot, "A portable fast sampling system for astronomical applications," in *Proc. URSI Gen. Assembly*. Maastricht, The Netherlands, 2002.

[21] M. L. Skolnik, *Introduction to Radar Systems*. New York: McGraw-Hill, 1980.

[22] T. Hagfors, "Remote probing of the Moon by infrared and microwave emissions and radar," *Radio Sci.*, vol. 5, pp. 189–227, 1970.

[23] H. Hiesinger, R. Jaumann, G. Neukum, and J. W. Head, "Ages of mare basalts on the lunar nearside," *J. Geophys. Res.*, vol. 105, no. E12, pp. 29 275–29 329, Dec. 2000.

[24] H. R. Hiesinger, J. W. Head, U. Wolf, R. Jaumann, and G. Neukum, "Ages and stratigraphy of mare basalts in Oceanus Procellarum, Mare Nubium, Mare Cognitum, and Mare Insularum," *J. Geophys. Res.*, vol. 108, no. E7, 1, 2003. DOI:10.1029/2002JE001985.

[25] W. D. Carrier, G. R. Olhoeft, and W. Mendell, "Physical properties of the lunar surface," in *Lunar Sourcebook*. New York: Cambridge Univ. Press, 1991.

[26] T. W. Thompson, J. B. Pollack, M. J. Campbell, and B. T. O'Leary, "Radar maps of the Moon at 70-cm wavelength and their interpretation," *Radio Sci.*, vol. 5, no. 2, pp. 253–262, 1970.

[27] C. M. Pieters, "Mare basalt types on the front side of the moon," in *Proc. Lunar Planet. Sci. Conf. 9*, 1978, pp. 2825–2849.

[28] T. W. Thompson, R. W. Shorthill, E. A. Whitaker, and S. H. Zisk, "Mare Serenitatis: A preliminary definition of surface units by remote observations," *Earth Moon, Planets*, vol. 9, no. 1/2, pp. 89–96, Mar. 1974.

[29] P. G. Lucey, D. T. Blewett, and B. D. Joliff, "Lunar iron and titanium abundance algorithms based on final processing of Clementine UV–visible images," *J. Geophys. Res.*, vol. 105, pp. 20 297–20 306, 2000.

[30] J. J. Gillis, B. L. Joliff, and R. C. Elphic, "A revised algorithm for calculating TiO_2 from Clementine UVVIS data: A synthesis of rock, soil, and remotely sensed TiO_2 concentrations," *J. Geophys. Res.*, vol. 108, no. E2, 2003. DOI:10.129/2001JE001515.

[31] B. A. Campbell and D. B. Campbell, "Regolith surface properties in the south polar region of the moon from 70-cm radar polarimetry," *Icarus*, vol. 180, no. 1, pp. 1–7, Jan. 2006.

[32] B. A. Campbell and J. Ward, *Dual-Polarization Calibrated Radar Map of the Moon*. NASA Planetary Data System, 2007. ARCB/NRAO-L-RTLS/GBT-4/5-70CM-V1.0.

Bruce A. Campbell (S'87–M'91) received the B.S. degree in geophysics from Texas A&M University, College Station, in 1986, and the Ph.D. degree in geology and geophysics from the University of Hawaii, Honolulu, in 1991.

Since 1992, he has been with the Center for Earth and Planetary Studies, Smithsonian Institution, Washington, DC. From 1996 to 1998, he was the Discipline Scientist for NASA's Planetary Instrument Definition and Development Program. His research interests focus on the applications of radar remote sensing to the understanding of volcanism, impact cratering, weathering, and other processes on terrestrial planets. Much of this work has emphasized the relationship of surface roughness to radar observations of volcanic surfaces, which remains a key element in interpreting data for Venus, the Moon, and Mars. Fieldwork in support of this includes the collection of a large database of high-resolution topographic profiles for lava flows in Hawaii and the desert southwest. More recent projects have expanded this effort to include radar penetration and polarization signatures of Mars-like sand, dust, and ash deposits. He is a team member for the SHARAD shallow radar sounder on the 2005 Mars Reconnaissance Orbiter. This instrument probes the upper kilometer of the martian crust to identify geologic layering and possible water or ice deposits.

Donald B. Campbell is currently a Professor of astronomy with Cornell University, Ithaca, NY. He has been using radar for over 30 years to study the surfaces of terrestrial planets, satellites, and smaller bodies in the solar system. He carried out some of the first detailed studies of the surface of Venus using the Arecibo radar system and was a coinvestigator on the Magellan mission. With colleagues, he discovered the unusual radar reflection properties of the surfaces of the icy Galilean satellites. Working with his graduate students, he has used the polarization properties of radar echoes to study the lunar regolith and mantling deposits on Venus, studied the wavelength dependence of radar reflections from the icy Galilean satellites to derive parameters of the scattering layer, and used radar interferometric techniques to measure the topography of the lunar poles. His current work includes radar studies of the surface of Titan and the icy midsized saturnian satellites, and high-resolution polarimetric radar studies of the surface of the Moon.

J. L. Margot, photograph and biography not available at the time of publication.

Rebecca R. Ghent, photograph and biography not available at the time of publication.

Michael Nolan, photograph and biography not available at the time of publication.

John Chandler, photograph and biography not available at the time of publication.

Lynn M. Carter received the B.S. degree in astronomy and physics from the University of Illinois, Urbana, in 1999 and the Ph.D. degree in astronomy from Cornell University, Ithaca, NY, in 2005.

She is currently a Postdoctoral Researcher with the Center for Earth and Planetary Studies, Smithsonian Institution, Washington, DC. Her primary research interest is in planetary geology, particularly the composition and structure of the surface and subsurface of Venus, Mars, Titan, the Moon, and asteroids. Her current research projects include ground-based radar studies of lunar pyroclastic deposits, using radar polarimetry to study the surface properties of asteroids, analysis of Cassini RADAR data of Titan to investigate the surface-scattering behavior, and using the SHARAD sounding radar on the Mars Reconnaissance Orbiter to study the extent and internal layering of martian volcanic deposits.

Nicholas J. S. Stacy, photograph and biography not available at the time of publication.